

Title

Subtitle

by

Mikkel Metzsch Jensen

THESIS

for the degree of

MASTER OF SCIENCE



Faculty of Mathematics and Natural Sciences
University of Oslo

Spring 2023

Title

Subtitle

Mikkel Metzsch Jensen

© 2023 Mikkel Metzsch Jensen

Title

<http://www.duo.uio.no/>

Printed: Reprosentralen, University of Oslo

Abstract

Abstract.

Acknowledgments

Acknowledgments.

Contents

List of symbols?

vii

1 Background Theory and Method	1
1.1 Tribology - friction	1
1.1.1 Macroscale	1
1.1.1.1 Amontons' law	1
1.1.2 Microscopic scale	2
1.1.2.1 Surface roughness - Asperity theories	2
1.1.3 Nanoscale - Atomic scale	3
1.1.3.1 Frenkel-Kontorova	4
1.1.3.2 Experimental procedures	8
1.1.3.3 (summary of) Expected frictional properties	9
1.2 Molecular Dynamics	10
1.2.1 Potentials	11
1.2.1.1 General formulation of potentials (?)	11
1.2.1.2 Lennard Jones	11
1.2.1.3 Stillinger weber	12
1.2.1.4 Tersoff	12
1.2.2 Integration	14
1.2.2.1 Velocity Verlet	14
1.2.3 Thermostats	15
1.2.3.1 Langevin thermostat	15
1.2.3.2 Implementing Langevin	18
1.2.4 MD limitations (?)	18
1.2.5 LAMMPS	18
1.3 Defining the system	18
1.3.1 Region definitions (Sheet, pullblocks and substrate)	18
1.3.2 Numerical procedure	20
1.3.3 Creating the sheet	21
1.3.3.1 Graphene	21
1.3.3.2 Indexing	21
1.3.3.3 Removing atoms	22
1.3.4 Kirigami patterns	23
1.3.4.1 Pop-up	23
1.3.4.2 Honeycomb	23
1.3.4.3 Random walk	23
1.4 Pressure reference	23
1.5 Fourier Transform (light)	24
1.6 Machine Learning (ML)	24
1.6.1 Feed forward network / Neural networks	25
1.6.2 CNN for image recognition	25
1.6.3 GAN (encoder + deoder)	25
1.6.4 Inverse desing using machine learning	25

1.6.5	Prediction explanation	25
1.6.5.1	Shapley	25
1.6.5.2	Lineariations	25
1.6.5.3	LRP	25
1.6.5.4	t-SNE	25

List of symbols?

Maybe add list of symbols and where they are used like Trømborg.

Chapter 1

Background Theory and Method

Small introtext to motivate this chapter. What am I going to go over here.

1.1 Tribology - friction

Friction is a part of the wider field tribology which includes the study of friction, wear and lubrication between two surfaces in relative motion [1, p. 1]. In this thesis we will only concern ourselves with so-called wearless dry friction. That is, without any use of lubrication and without any resulting wear of the contacting surfaces. Tribological systems take place across a broad range of time and length scales, ranging from geological stratum layers involved in earthquakes [2] to microscopic atomistic processes, as in the gliding motion of a nanocluster of a nanomotor [3]. This vast difference in scale gives rises to different frictional mechanism being dominating at different scales. On a macro scale the system is usually subject to relatively high loads and speeds leading to high contact stresses and wear. On the other hand, the micro-/nanoscale regime occupies the opposite domain operating under relatively small loads and speeds with negligible wear [2] [4, p. 5]. While macroscale friction is often reduced into a few variables such as load, material type, speed and surface roughness it is clear that the micro-/nanoscale friction cannot be generalized under such a simple representation. On the micro-/nanoscale the tribological properties dominated by surface properties which will introduce an additional sensitivity variables such as temperature, humidity and even sliding history. The works of Bhushan and Kulkarni [5, (1996)] showed that the friction coefficient decreased with scale even though the materials used was unchanged. This reveals an intrinsic relationship between friction and scale as the contact condition is altered.

The phenomenological descriptions of macroscale friction cannot yet be derived from the fundamental atomic principles, and bridging the gap between different length scales in tribological systems remains an open challenge [3]. Hence, the following sections will be organized into macro-, micro- and nanoscale representing the theoretical understanding governing each scale regime. While our study of the graphene sheet is based on a nanoscale perspective the hypothesizing about application possibilities will eventually draw upon a macroscale perspective as well. Thus, we argue that a brief theoretical introduction to all three major scales is of high interest for a more complete interpretation of the findings in this thesis.

1.1.1 Macroscale

Our working definition of the *macroscale* is everything on the scale of visible everyday objects, which is usually denoted to the size of millimeters 10^{-3} m and above. Most importantly, we want to make a distinction to the *microscale*, where the prefix indicates the size of micrometers m^{-6} , and hence we essentially assign everything larger than *micro* to the term *macroscale*¹.

1.1.1.1 Amontons' law

In order to start and keep a solid block moving against a solid surface we must overcome certain frictional forces F_{fric} [1]. The static friction force F_s corresponds to the minimum tangential force required to initiate the sliding

¹The width of a human hair is on the length scale 10^{-5} to 10^{-4} m which constitute a reasonable boundary between macro- and microscale which fit well with a lower bound of human perception capabilities.

while the kintec friciton force F_k corresponds to the tangential force needed to sustain such a sliding at steady speed. The work of Leonardo da Vinci (1452–1519), Guillaume Amontons (1663–705) and Charles de Coulomb (1736–1806) all contributed to the empirical law, commonly known as Amontons' law, which is a common friction model for the macroscale regime. Amontons' law states that the fricitonal forces is entirely independent of contact area and sliding velocity (at ordinary sliding velocities). Instead, it relies only on the normal force² F_N , acting perpendicular to the surface, and the material specific friction coefficient μ as

$$F_{\text{fric}} = \mu F_N. \quad (1.1)$$

The friction coefficient is typically different for the cases of static (μ_s) and kinetic (μ_k) friction, usually with values lower than one and $\mu_s \geq \mu_k$ in all cases [1, p. 6].

Allthough Amontons' law has been succesfull in the modelling of macroscale friction it has its limitations. For instance, it was later discovered that the static friction is not independent of time. It depends on the so-called contact history with increasing friction as the logarithm of time of stationary contact [6]. For the kinetic friction the independency of sliding velocity disappears at low velocities as thermal effects becomes important and for high velocities due to inertial effetc. [1, pp. 5-6].

Additionally, due to the emperical foundation, Amontons' law does not provide a physical insight into the underlying mechanisms of friction. However, as we will later discuss in more detail, we can understand the overall phenomena of friction through statistical mechanics by the concept of *equipartition of energy* [3]. A system in equilibrium has its kinetic energy uniformly distributed among all its degrees of freedom. When a macroscale object is sliding in a given direction it is clearly not in equilibrium since one of its degrees of freedom carriers considerable more kinetic energy. Thus, the system will have a tendency to transfer that kinetic energy to the remaining degrees of freedom as heat. This heat will dissipate to the sourroundings and the object will slow down as a result. Hence, friction is really just the tendency of going toward equilibrium energy equipartitioning among many interacting degrees of freedom [3]. From this point of view it is clear that friction is an inevitable part of contact physics, but even though friction can be removed altogether, we are still capable of manipulating it in usefull ways.

The attentive reader might point out that we have already moved the discussion partly into the microscopic regime as *statistical mechanics* generally aim to explain macroscale behaviour by microscopic interactions. In fact this highlight the nessecity to consider smaller scales in order to achieve a more in depth understadning of friction.

1.1.2 Microscopic scale

Going from a macro- to microscale perspective, a length scale of order 10^{-6} m, it was realized that most surfaces is in fact rough [7]. The contact between two surfaces consist of numerous smaller contact point, so-called asperities, for which the friction between two opposing surfaces involves interlocking of those asperities as visualized in figure 1.1. It is generally accepted that friction is caused by two mechanism: mechanical friction and chemical friction [2]. The mechanical friction is the “plowing” of the surface by hard particles or said asperities with an energy loss associated attributed deformations of the asperity. While plastic deformations, corresponding to wear, is obviously expected to act as an energy sink, elastic deformations is also sufficient in explaining energy loss due to phonon excitations. The chemical friction arrises from adhesion between microscopic contacting surfaces, with an energy loss assigned to breaking and forming of bonds.

1.1.2.1 Surface roughness - Asperity theories

Asperity theories are based on the observation that microscopic rough surfaces, with contacting asperities each with a contact area of A_{asp} , will have a true contact area $\sum A_{\text{asp}}$ much smaller than the apperent macrosopic area A_{macro} [2]. The friction force was shown to be proportional to the true contact area as

$$F_{\text{fric}} = \tau \sum A_{\text{asp}},$$

where τ is an effective shear strength of the contacting bodies. Note that this is still compatible with Amontons' law in eq. (1.1) if we find a linear relationship between the real contact area and the applied normal force F_N . In

²Normal force is often used interchangeably with the terms *load* and *normal load*.

figure 1.1 we see a visualization on how the contact area might intuitively increase with normal force as the asperity tips is deformed into broader contact points.

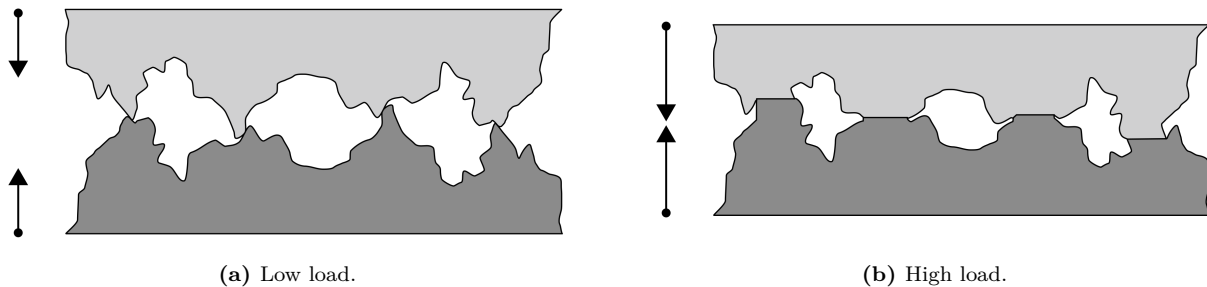


Figure 1.1: Qualitatively illustration of the microscopic asperity deformation under increasing load from frame a to b [8].

Many studies have focused on single asperity contacts to reveal the relationship between the contact area and F_N (13-15 from [7]). By assuming perfectly smooth asperities, with radii of curvature from micrometers all the way down to nanometers, continuum mechanics can be used to predict the deformation of asperities as normal force is applied. A model for non-adhesive contact between homogenous, isotropic, linear elastic spheres was first developed by Hertz (17 from [7]), which predicted $A_{\text{asp}} \propto F_N^{2/3}$. Later adhesion effects were included in a number of subsequent models, including Maugis-Dugdale theory (18 from [7]), which also predicts a sublinear relationship between A_{asp} and F_N . Thus, the common feature of all single-asperity theories is that A_{asp} is a sublinear function of F_N , leading to a similar sublinear relationship for $F_{\text{fric}}(F_N)$, which fails to align with the macroscale observations modelled by Amontons' law (eq. (1.1)).

A variety of multiasperity theories has attempted to combine single asperity mechanics by statistical modelling of the asperity height and spatial distributions [9]. This has led to ... a linear relationship between A_{asp} and F_N . Unfortunately, these results are restricted in terms of the magnitude of the load and contact area, where multiasperity contact models based on the original ideas of Greenwood and Williamson [10] only predicts linearity at vanishing low loads, or Persson [11] which works for more reasonable loads but only up to 10-15 % of the macroscale contact area. However, as the load is further increased all multiasperity models predict the contact area to fall into the sublinear dependency of normal force as seen for single asperity theories [9].

1.1.3 Nanoscale - Atomic scale

Going from a micro- to nanoscale, on the order of 10^{-9} meter, it has been predicted that continuum mechanics will break down [12] due to the discreteness of individual atoms. Note that atom spacing lies in the domain of a few ångströms Å (10^{-10} m) and thus we take the so-called corresponding atomic-scale to be a part of the nanoscale regime. In a numerical study by Mo et al. [7] (considering asperity radii of 5-30 nm) it has been shown that the asperity area A_{asp} , defined by the circumference of the apparent asperity contact zone, is in fact sublinear with F_N . This is accommodated by the observation that not all atoms within the circumference make chemical contact with the substrate. By modelling the real area $A_{\text{real}} = N A_{\text{atom}}$, where N is the amount of atoms within the range of chemical interaction range and A_{atom} is the associated atom surface area, they found a consistent linear relationship between friction and the real contact area. Without adhesive forces this lead to a similar linear relationship $F_{\text{fric}} \propto F_N$, while adding van der Waals adhesion to the simulation gave a sublinear relationship, even though the $F_{\text{fric}} \propto A_{\text{real}}$ was maintained.

This result emphasizes that contact area is still expected to be play a major role on the nanoscale for asperity theory. It is simply the definition of contact area that undergoes a change when transitioning from micro- to nanoscale. However, considering the simulation setup of our numerical study, a flat sheet on a flat substrate, it is unfounded to rely on asperity theories. With no asperities present it is unknown (I could not find any articles on contact area for nanoflakes) whether the real contact area continue to be dominant part of the friction mechanism at play. Before diving into alternative theoretical approaches to address this issue we point out that we might in fact be able to introduce an ensemble of asperities through a strategic combination of kirigami inspired cuts and stretching of the sheet. Hence, we might hypothesize that such a transition will contribute to significant change in the governing mechanism of friction in the system which we attempt to optimize for

certain properties.

In the lack of noteworthy structural asperities on, the friction can instead be modelled as a consequence of the rough potential of the atomic landscape. A series of models builds on this idea by considering different ways for the atoms to interact interatomic, with the moving body and the substrate surface. In figure 1.2 three major models 1D models is displayed. The time-honored Prandtl-Tomlinson (PT) model describes a point-like tip sliding over a space-periodic fixed crystalline surface with a harmonic coupling to the *moving body*. This is analog to that of an experimental cantilever (experimental name). Further extensions was added in the Frenkel-Kontorova (FK) model by substituting the tip with a chain of harmonic coupled atoms dragged from the end (I am not sure that the figure is correct here by drawing a spring), and finally combined in the Frenkel-Kontorova-Tomlinson (FKT) with the addition of a harmonic coupling between the chain and the moving body.

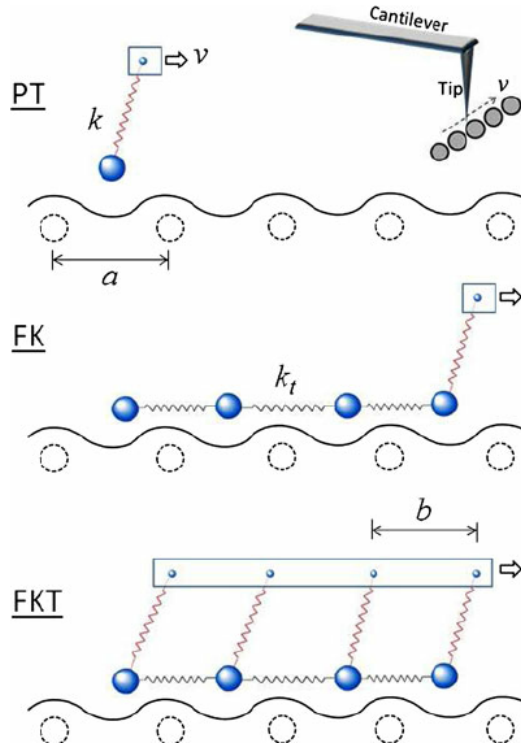


Figure 1.2: Temporary figure from https://www.researchgate.net/figure/Illustrations-of-the-1D-PT-FK-and-FKT-models-Large/fig1_257670317

1.1.3.1 Frenkel-Kontorova

The standard Frenkel-Kontorova (FK) model consists of a 1D chain of N classical particles of equal mass, representing atoms, interacting via harmonic forces and moving in a sinusoidal potential as sketched in figure 1.3. The hamiltonian is

$$H = \sum_{i=1}^N \left[\frac{p_i^2}{2m} + \frac{1}{2} K(x_{i+1} - x_i - a_c)^2 + \frac{1}{2} U_0 \cos\left(\frac{2\pi x_i}{a_b}\right) \right], \quad (1.2)$$

where the atoms are labelled sequentially $i = 1, \dots, N$. The first term $p_i^2/2m$ represents the kinetic energy with momentum p_i and mass m . Often the effects of inertia are neglected, referred to as the static FK model, while the inclusion, as shown in eq. (1.2), is known as the dynamic FK model [13]. The next term describes the harmonic interaction with elastic constant K , nearest neighbour distance $\Delta x = x_{i+1} - x_i$ and corresponding nearest neighbour equilibrium distance a_c . The final term represents the periodic substrate potential (external potential on site) with amplitude U_0 and period a_b . Different boundary choices can be made where both free

ends nad periodic conditions gives reasonable results. The choice of fixed ends however makes the chain incapable of sliding.

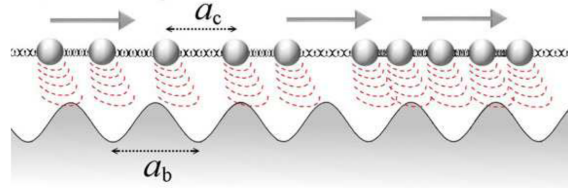


Figure 1. A sketch of the FK model, showing the two competing lengths: the average interparticle spacing and the lattice periodicity of the substrate.

Figure 1.3: [Temporary figure from [3]]

To probe static friction one can apply an external force which increases adiabatically until sliding accours. This corresponds to the static FK model and it turns out that the sliding properties are entirely governed by its topological excitations referred to as so-called *kinks* and *antikinks*

Commensurability We can describe the frictional behvaiour in terms of commensurability, that is, how well the spacing of the atoms match the periodic substrate potential. We describe this by the length ratio $\theta = a_b/a_c = N/M$ where M denotes the number of minemas in the potential (within the length of the chain). A rational number for θ means that we can align the atoms in the chain perfectly with the minemas, without stretching the chain, corresponding to a *commensurate* case. If θ is irrational the chain and substrate cannot fully align, and we denote this as being *incommensurate*.

We begin with the simplest commensurate case of $\theta = 1$ where the spacing of the atoms matches perfectly the substrate potential periodicity, i.e. $a_c = a_b$, $N = M$. The ground state (GS) is the configuration where each atom fits in one of the substrate minema. By adding an extra atom we would effectively shift over some atoms, away from these ideal state, giving rise to a kink excitation, i.e. two atoms will have to share the same potential corrugation as sketched in figure 1.5. On the other hand, removing an atom from the chain results in a antikink excitation where one potential corrugation will be left “atomless”. In order to reach a local minimum the kink (antikink) will expand in space over a finite length such that the chain undertakes a local compression (expansion). When applying a tangential force to the chain it is much easier for a kink to move along the chain than it is for the non-excited atoms since the activation energy ϵ_{PN} for a kink displacement is systematically smaller (often much smaller) than the potential barrier U_0 . Thus, the motion of kinks (antikinks), i.e. the displacement of extra atoms (atom vacancies), is represententing the fundamental mechanism for mass transport. These displacements is responsible for the mobility, diffusivity and conductivity within this model.

In the ideal zero temperature commensurable case with an adiabatical increase in force, all atoms would be put into an accelerating motion as soon the lowest energy NU_0 is present. However, in reality any thermal excitation would excite the system before this point is reached by the creation of kink-antikink pairs that would travel down the chain. For a chain of finite length these often accrour at the end of the chain running in opposite direction. As a kink travels down the chain the atoms is advanced by one atom spacing a_b along the substrate potential. This cascade of kink-antikink exications is shown in figure 1.4

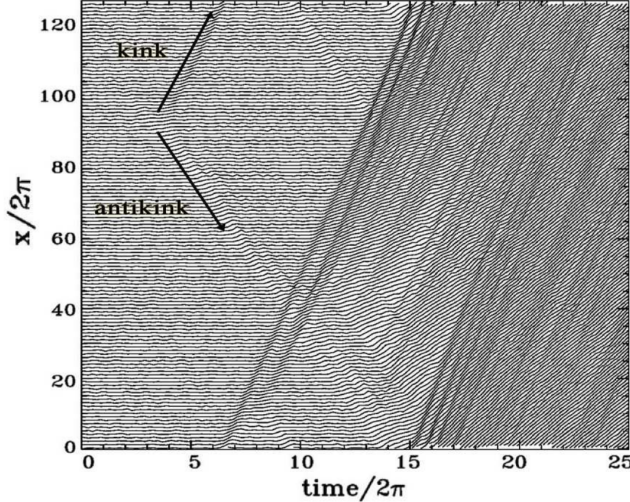


Figure 2. Time dependence of the atomic trajectories for the fully matched ($\theta = 1$) FK model at the (low-temperature) onset of depinning. Motion starts with the nucleation of a kink-antikink pair. The kink and the antikink depart in opposite directions cross the periodic boundary conditions, and collide quasielastically. A second kink-antikink pair forms in the wake of the initial kink. Further kink-antikink pairs are generated, with an avalanche-like increase of the kink-antikink concentration, eventually leading to a sliding state. Adapted from Ref. [21], Copyright (1997) by The American Physical Society.

Figure 1.4: **Temporary** figure from [3]

For the 2D case where an island is deposited on a surface, in our case the graphene sheet on the Si substrate, we generally also expect the sliding to be initiated by kink-antikink pairs at the boundary.

For the case of incommensurability, i.e. $\theta = a_b/a_c$ is irrational, the GS is characterized by a sort of ‘‘staircase’’ deformation. That is, the chain will exhibit regular periods of regions where the chain is slightly compressed (expanded) to match the substrate potential, separated by kinks (antikinks), where the increased stress is eventually released through a localized expansion (compression) as illustrated in figure 1.5 Go though this again and make sure that I got the compression expansion directions rihgt....



Figure 1.5: **Temporary** figure from [urlhttp://www.iop.kiev.ua/~obraun/myreprints/surveyfk.pdf](http://www.iop.kiev.ua/~obraun/myreprints/surveyfk.pdf) p. 14. Incommensurable case ($\theta = ?$) where atoms sits slightly closer than otherwise dictated by the substrate potential for which this regularly result in a kink here seen as the presence of two atoms closeæy together in on of the potential wells.

The incommensurable FK model contains a critical elastic constant K_c , such that for $K > K_c$ the static friction F_s drops to zero, making the chain able to initiate a slide at no energy cost, while the low-velocity kinetic friction is dramatically reduced. This can be explained by the fact that the displacement accouring in the incommensurable case will yield just as many atoms climbing up a corrugation as there are atoms climbing down. For an infinite chain this will exactly balance the forces making it non-resistant to sliding. Generally, incommensurability guarantees that the total energy (for $T = 0$) is independent of the relative position to the potential. However, when sliding freely a single atom will eventually occupy a maximum of the potential. When increasing the potential magnitude U_0 or softning the chain stiffness, lowering K , the possibility to occupy such a maximum is no longer present. This marks the so-called Aubry transition at the critical elasic constant

$K = K_c(U_0, \theta)$ where the chain goes from a free sliding to a *pinned state* with a nonzero static friction. K_c is a discontinuous function of the ratio θ , due to the reliance on irrational numbers for incommensurability. The minimal value $K_c \simeq 1.0291926$ in units $[2U_0(\pi/a_b)^2]$ is achieved for the golden-mean ratio $\theta = (1 + \sqrt{5}/2)$. Notice that the pinning is provided despite translational invariance due to the inaccessibility to move past the energy barrier which act as dynamical constraint. The Aubry transistion can be invistigated as a first-order phase transistion for which power laws can be defined for the order parameter. This is beyond the scope of this thesis as we merely are going to point to the FK model for the understanding of stick-slip behvaiour and the concept of commensurability.

The phenonema of non-pinned configurations is named *superlubricity* in tribological context. Despite the misleadning name this referses to the case where the static friction is zero while the kinetic friction is nonzero but reduced. For the case of a 2D sheet it is possible to alter the commensurability by changing the orientation of the sheet relative to the substrate. This has been shown for a graphene flake (single layer) sliding over a graphite surface (multiple layers) [14]. In figure 1.6 we see how the friction depends on the relative orientatin between the sheet and substrate.

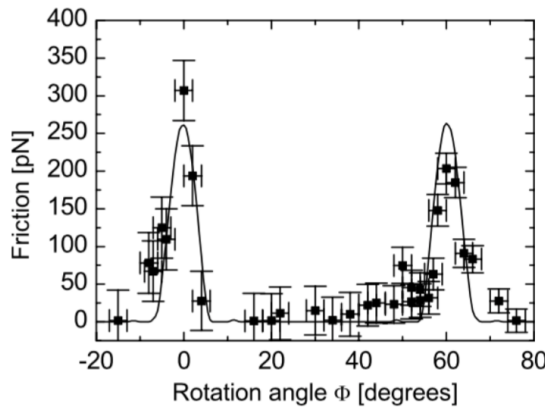


Fig. 6. Average friction force versus rotation angle Φ of the graphite sample around an axis normal to the sample surface. Two narrow peaks of high friction are observed at 0° and 61° , respectively. Between these peaks a wide angular range with ultra-low friction, close the detection limit of the instrument, is found. The first peak has a maximum friction force of 306 ± 40 pN, and the second peak has a maximum of 203 ± 20 pN. The curve through the data points shows results from a Tomlinson model for a symmetric 96-atom graphite flake sliding over the graphite surface (for details about the calculation see [39]).

Figure 1.6: [Temporary] figure from [14] showing superlubricity for incommensurable orientations between graphene and graphite. [temporary]

Kinetic friction In the FK model the kinetic friction is primarily caused by resonance between the sliding induced vibrations and phonon modes in the chain [13]. When all atoms are sliding rigidly width center of mass velocity v_{CM} the atoms will pass the potential maxima with the so-called *washboard frequency* $\Omega = 2\pi v_{CM}/a_b$. For a weak coupling between the chain and the potential we can use the zero potential case as an approximation for which the known dispersion relation for the 1D harmonic chain is given [Kittel]

$$\omega_k = \sqrt{\frac{4K}{m}} \left| \sin \left(\frac{k}{2} \right) \right|,$$

where ω_k is the phonon frequency and $k = 2\pi i/N$ the wavenumber with $i \in [N/2, N/2]$. Strong resonance will accour if Ω is close to the frequency of the phonon modes ω_q in the chain with wavenumber $q = 2\pi a_c/a_b = 2\pi\theta^{-1}$

or its harmonics nq for $n = 1, 2, 3, \dots$ [15]. Thus, we can approximate the resonance speed as

$$\begin{aligned} n\Omega &\sim \omega_{nq} \\ n\frac{2\pi v_{CM}}{a_b} &\sim 2\sqrt{\frac{K}{m}} \left| \sin\left(\frac{2n\pi\theta^{-1}}{2}\right) \right| \\ v_{CM} &\sim \frac{\sin(n\pi\theta^{-1})}{n\pi} \sqrt{\frac{Ka_b^2}{m}}. \end{aligned}$$

When the chain slides with a velocity around resonance speed, the washboard frequency can excite acoustic phonons which will dissipate to other phonon modes as well. At zero temperature the energy will transform back and forth between internal degrees of freedom and center of mass movement of the chain. Hence, at zero temperature this will indeed speed up the translation decay (decay is synonymous for translational movement right?). However, for the more realistic case of non-zero temperature the substrate serves as a thermostat for which energy will dissipate from the chain to the substrate degrees of freedom giving rise to kinetic friction. On the other hand, this predicts that certain sliding speed, which does not induce phonon resonance, will be subject to extremely low kinetic friction. This is strongly connected to the superlubricity term although this phonon dynamics is simplified in this 1D model.

A common way to model the non-zero temperature case is by the use of a Langevin thermostat, which simulates the dissipation by adding a viscous damping force and thermal fluctuations by the addition of Gaussian random forces with variance proportional to the temperature (This is covered in more details in section 1.2.3.1). In combination, this gives rise to a kinetic friction that is both velocity and temperature dependent.

By extending the FK model into 2D [13] it can be shown numerically that the friction coefficient generally increases with increasing velocity and temperature respectively.

Temperature dependence Might find something interesting here [16] or [17].

Smooth sliding Find a suitable place to introduce smooth sliding. Above certain velocities the stick-slip motion disappears. [1, p. 142-ish]

1.1.3.2 Experimental procedures

[1]

Experimentally nanoscale friction is challenging to approach as the forces, on the scale of nano-newtons as well, is extremely small. Additionally surface topography is not easily viewed. On the other side simulations provide full transparency regarding information of the physical structure of the sample along with forces, velocities and temperature. However, in order to compare numerical results the experimental procedures is most often mirrored in simulations. Thus it is beneficial to address the most common experimental techniques when designing a simulation.

Scanning Probe Microscopy Scanning probe microscopy (SPM) includes a variety of experimental methods which is used to examine surfaces with atomic resolution [18, p. 6-]. This was originally developed for surface topography imaging, but today it plays a crucial role in nanoscale science as it is used for probe-sampling regarding tribological, electronic, magnetic, biological and chemical character. The family of methods involving the measurement of forces is generally referred to as *scanning force microscopies* (SFM).

One such method arose from the *atomic force microscope*, which consists of a sharp micro-fabricated tip attached to a cantilever force sensor, usually with a sensitivity below 1 nN. The force is measured by recording the bending of the cantilever, either as a change in electrical conduction or more commonly, by a light beam reflected from the back of the cantilever into a photodetector [1]. By adjusting the tip-sample height to keep a constant normal force while scanning across the surface this can be used to produce a surface topography map. By tapping the material (dynamic force microscopy) with sinusoidally vibrated tip the effects from friction and other disturbing forces can be minimized in order to produce a clear image (including example, preferable of graphene). However, when scanning perpendicularly to the cantilever axis one is also able to measure the frictional force as torsion of the cantilever. By having four quadrants in the photodetector (as shown in figure 1.7), one can simultaneously measure the normal force and friction force as the probe scans across the surface.

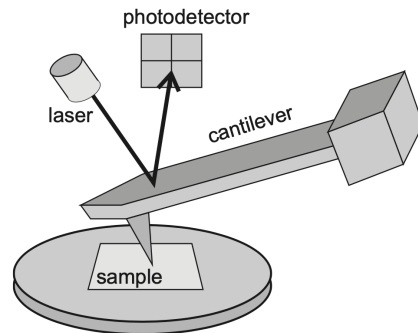


Figure 17.1 Schematic diagram of a beam-deflection atomic force microscope.

Figure 1.7: **Temporary** figure from [1, p. 184]

This can also be used to drag a nanoflake as done by Dienwiebel et al. [14] (earlier referenced), where a graphene flake was attached to a FFM tip and dragged across graphite.

Surface Force Apparatus (SFA) Is this the one where two surfaces slide in opposite direction (at least that is the common MD way I see it.)

1.1.3.3 (summary of) Expected frictional properties

The setup of our simulation is most reminiscent of a graphene flake sliding on a substrate. This has been studied numerically in molecular dynamic simulations by Zhu and Li [19, 2018] for a graphene flake on a gold substrate and by Zhang et al. [20](2019) on a diamond substrate, and in a tight-binding simulation by Bonelli et al. [21](2009) for graphene on graphite. Experimental studies of a graphene flake attached to a AFM is done by Dienwiebel et al. [14, 2005] and Feng et al. [22, 2013] sliding on graphite, but these are mainly concerned with superlubricity as a function of flake orientation commensurability.

In our study we simulate a graphene flake on a silicon substrate which deviates slightly from the above-mentioned reference. Additionally, the normal force is only applied to the ends of the sheet. Obviously stretching and cutting the sheet will separate our study dramatically from the references, but we aim to compare the frictional properties to the reference before applying stretch or cuts.

Qualitatively we have the following expectations for the unstretched and non-cut graphene sheet.

Qualitatively

1. Stick slip: Generally expect to see periodic stick-slip motion with a period matching the lattice constant(s) involved [7]. This was both present in the MD simulations [19], [20] and in the experiment by [14]. In AFM and SFA experiments, the stick-slip motion tends to transition into smooth sliding when the speed exceeds $\sim 1\mu\text{ m/s}$ while in MD modelling the same transition is observed in the $\sim 1\text{m/s}$ region [3]. This order of magnitude discrepancy has been largely discussed in connection to simplifying assumptions in MD simulations. Bonelli et al. [21] found that the stick-slip behaviour was present when the cantilever-tip-flake coupling was done with a relatively soft springs in contrast to hard springs which inhibited it.
2. Static friction: As highlighted in the FK model static friction will be sensitive to commensurability, which will additionally be affected by flake size. Reguzzoni and Righi [23] have shown that the effective commensurability will increase drastically below a critical flake radius on the order of 10 \AA . Macroscopically we expect to see a logarithmic increase in friction with time [6], and hence due to the short time-span of the static contact before dragging, it is not easy to estimate whether a significant static friction peak will be found.
3. Orientation (friction anisotropy): As predicted by the FK model and confirmed both numerically [19], [20] and experimentally [14], [22] we expect to see a dependence of friction force on orientation due to changing commensurability. Zhu and Li [19] (gold substrate) reported the highest friction when sliding

along the armchair direction, while Zhang et al. [20] (diamond substrate) found the zigzag-direction to give the highest friction force along the zigzag direction (also the most evident stick-slip behaviour).

Table 1.1: Quantitative nano friction dependence on various variables.

Variable	Dependency	Numerical studies	Experimental
Normal force F_N	$F_{\text{fric}} \propto F_N^\alpha$ $\alpha \leq 1$	Zhang et al. [20] finds a seemingly linear relationship $F_{\text{fric}} \propto F_N$ while Bonelli et al. [21] reports a sublinear relationship. The latter corresponds with that of nanosasperity simulations where [7] (amorphous carbon tip and a diamond sample) also found sublinear relationship when including adhesion.	Experimentally different trends have been observed [1, p. 200]. For the graphebne flake Dienwiebel et al. [14] found a non-dependent relationship while Feng et al. [22] did report on this. FFM analog to the single asperity setup have yielded both linear relationship [24] (silicon tip on gold) while Schwarz et al. [25] found that FFM with well-defined spherical tips matched with theoretical results(DMT, elastic spheres pressed together [1, p. 200]), yielding a power law $F_{\text{fric}} = F_N^{2/3}$.
Velocity v	$F_{\text{fric}} \propto \ln v$		Logaritmic velocity dependence of friction has been measured for nanotip friction [1, p. 201] associated to thermal activation and possibly the time available to form bond between the tip and the substrate. At higher velocities thermally activated processes are less important and friction becomes independent of velocity. This has been observed for Si tips and diamond, graphite and amorphous carbon surfaces with scan velocities above $1 \mu\text{m}/\text{s}$.
Temperature T	Either increase (MD) or decrease as $F_{\text{fric}} \propto \exp(1/T)$ (experimental)	Zhang et al. [20] found tha friction increased with temperature.	Zhao et al. [16] found $F_{\text{fric}} \propto \exp(1/T)$
Real contact area A	$F_{\text{fric}} \propto A$	Mo et al. [7] found that $F_{\text{fric}} \propto A$ where A is the real contact area defined by atoms within chemical range. This is not studied for the case of a nanoflake where the contact area is presumably rather constant.	

1.2 Molecular Dynamics

Maybe read “Computer Simulations 7 of Nanometer-Scale Indentation and Friction” from [18]
Read [3][p. 18]

A promising compromise could possibly be provided by the so-called reactive potentials [120–122], capable of describing some chemical reactions, including interface wear with satisfactory computational efficiency in large-scale atomic simulations, compared to semi-empirical and first-principles approaches. [3]

- MD simulation (classical or ab initio)
- Basics of classical MD simulations: Integration and stuff
- Ab initio simulation (quantum mechanics, solving schrödinger)

1.2.1 Potentials

The choices of potentials used in the MD simulation is mainly based on the on [26] which have a somewhat similar MD friction simulation, the difference being that they impose a Si-tip on the graphene sheet supported by a Si-substrate where we impose drag the whole sheet upon the substrate. Nonetheless this serves as a good anchor for the methodology of the setup. The covalent bonds of C-C in graphene and Si-Si in the substrate is described by the Tersoff and Stillinger–Weber potentials, respectively. A typical 12-6 Lennard–Jones potential is used to describe the van der Waals adhesive interaction between graphene and the substrate.

1.2.1.1 General formulation of potentials (?)

On a general note we can generalize the n-body potential as the expansion in orders of participating atoms as

$$E = \sum_i V_1(\mathbf{r}_i) + \sum_{\substack{i,j \\ i < j}} V_2(\mathbf{r}_i, \mathbf{r}_j) + \sum_{\substack{i,j,k \\ i < j < k}} V_3(\mathbf{r}_i, \mathbf{r}_j, \mathbf{r}_k) + \dots$$

where \mathbf{r}_n is the position of the n th particle and V_m is called an m -body potential [27]. The first one-body term corresponds to an external potential, followed by the two-body term, the three-body term and so on. The simplest model that includes particle interaction is the pair potential truncating the expansion after the two-body term. A general feature of the pair potentials is that they favor close-packed structures which is unsuited to describe covalent bonds that take more open structures. In particular, pair potentials are completely inapplicable to strongly covalent systems such as semiconductors [27]. In order to accomodate the description of covalent bonds the natural step is thus to include the next step of the expansion, the three-body terms, as we will see for the modeling of the graphene sheet C-C bonds and the Silicon sheet Si-Si bonds. For the interaction between the sheet and the substrate we can nojes med a Lennard Jones pair potential describing the non-bonded van der Waals interaction.

1.2.1.2 Lennard Jones

This sections is based on [[28], [29], [30]].

The Lennard-Jones (LJ) model is probably one of the most famous pair potentials used in MD simulations. LJ models the potential energy between two non-bonding atoms based solely on interatomic distance r . The model accounts for attractive forces arising from dipole-dipole, dipole-induced dipole and London interactions, and repulsive forces that capture the hard core (is this safe to say?) of overlapping wave functions at small distances. Thus it is assumed neutrally charged atoms and was originally proposed for noble gases. The classical 12-6 version of the model (refering to the power law of the repulsive and attractive forces respectively) reads

$$E = 4\epsilon \left[\left(\frac{\sigma}{r} \right)^{12} - \left(\frac{\sigma}{r} \right)^6 \right], \quad r < r_c, \quad (1.3)$$

where r is the interatomic distance with cut-off r_c , ϵ is the depth of the potential well and σ the distance where the potential is zero. By solving for the potential minimum ($dE/dr = 0$) we find the equilibrium distance to be $r_0 = \sigma^{1/6}$. This makes for an even cleary interpretation of σ which effectively sets the equilibrium distance between atoms, i.e. the dividing line for which the net force is repulsive or attractive. While the LJ model in many ways is an oversimplified model that is insufficient in its description of ... (get source and concrete examples) it is commonly used as a model for intermaterial interactions (between moving object and substrate) in friction studies [[26], [31], [2]].

1.2.1.3 Stillinger weber

This section is based on [[32], [33]]

The stillinger weber potential takes the form of a three body potential

$$E = \sum_i \sum_{j>i} \phi_2(r_{ij}) + \sum_i \sum_{j\neq i} \sum_{k>j} \phi_3(r_{ij}, r_{ik}, \theta_{ijk}),$$

where r_{ij} denotes the distance between atom i and j and θ_{ijk} the angle between bond ij and jk . The summations is over all neighbours j and k of atom i within a cut-off distance $r = a\sigma$.

The two-body term ϕ_2 builds from the LJ model with the addition of an exponential cutoff term

$$\phi_2(r_{ij}) = A_{ij}\epsilon_{ij} \left[B_{ij} \left(\frac{\sigma_{ij}}{r_{ij}} \right)^{p_{ij}} - \left(\frac{\sigma_{ij}}{r_{ij}} \right)^{q_{ij}} \right] \exp\left(\frac{\sigma_{ij}}{r_{ij} - a_{ij}\sigma_{ij}}\right). \quad (1.4)$$

The model parameters A , ϵ , B , σ , p , q and a comes with i, j indices to indicate that theese parameters should be specified for each unique pair of atom types. However, in our case we will only provide a single value for each model parameter as we are exclusively dealing with Si-Si bonds. We see that the first term in eq. (1.4) is reminiscent of the LJ model in eq. (1.3) while the last term effectively drives the potential to zero at $r = a\sigma$, which is thus the chosen cut-off distance for the potential evaluation. With the model parameters for the Si-Si modelling (see table 1.2) the cut-off becomes ~ 3.8 Å.

The three body term includes an angle dependency as

$$\phi_3(r_{ij}, r_{ik}, \theta_{ijk}) = \lambda_{ijk} \epsilon_{ijk} \left[\cos \theta_{ijk} - \cos \theta_{0,ijk} \right]^2 \exp\left(\frac{\gamma_{ij}\sigma_{ij}}{r_{ij} - a_{ij}\sigma_{ij}}\right) \exp\left(\frac{\gamma_{ik}\sigma_{ik}}{r_{ik} - a_{ik}\sigma_{ik}}\right), \quad (1.5)$$

where $\theta_{0,ijk}$ is the equilibrium angle. The first term of eq. (1.5) includes an angle dependency analog to a harmonic oscillator based on a cosine angle distance from the equilibrium angle. The final two terms act again as a cut-off function by driving the potential to zero at $r_{ij} = a_{ij}\sigma_{ij}$ and $r_{ik} = a_{ik}\sigma_{ik}$ respectively.

The parameters used for the Si-Si bond modeling is displayed in table 1.2 along with an interpretation of each model parameter.

Table 1.2: Parameters for the stilliner weber potential used for intermolecular interactions in the silicon substrate.

Parameter	Value	Description
ϵ	2.1683	Individual depth of the potential well for each atom type pair/tiplets.
σ	2.0951	Distance for which the individual pair interactions has zero potential (analog to the LJ model).
a	1.80	The individual cut-off distance for each atom type pair.
λ	21.0	The overall depth of the three-body potential well.
γ	1.20	The shape of the three-body cut-off terms.
$\cos(\theta_0)$	-1/3	Cosine of equilibrium angle.
A	7.049556277	The overall depth of the two-body potential well.
B	0.6022245584	Scales the repulsion part of the two-body term.
p	4.0	The power dependency for the repulsion part of the two-body term.
q	0.0	The power dependency for the attraction part of the two-body term.
tol	0.0	LAMMPS: Option to define a different cut-off than the theoretical of $r = a\sigma$. $tol = 0$ refers to the theoretical being used.

1.2.1.4 Tersoff

This section is based on [[34], [27]].

The tersoff potential abandon the idea of a general n -body form and attempts instead to build the model on a more physics informed approach; The more neighbours an atom has the weaker the bonds will be. Thus it introduces the bond order (bond strength), that is environment specific and decrease with increasing bond coordination (number of neighbours for a given atom). The potential energy is taken to have the form

$$E = \sum_i E_i = \frac{1}{2} \sum_{i \neq j} V_{ij},$$

$$V_{ij} = f_C(r_{ij}) [f_R(r_{ij}) + b_{ij} f_A(r_{ij})],$$

where the total potential energy is decomposed into a bond energy V_{ij} . The indices i and j run over the atoms of the system with r_{ij} denoting the distance between atom i and j . Notice that the sum includes all combinations of i, j where $i \neq j$ meaning that the same bond is double counted which is the reason for the additional factor 1/2. The reasoning behind comes from the asymmetry of the bond order $b_{ij} \neq b_{ji}$ leading to a $V_{ij} \neq V_{ji}$. The bond energy is composed of a repulsive term f_R , arising from overlapping wave functions, and an attractive term f_A associated with bonding. f_C is simply a smooth cut-off function to increase computational efficiency. b_{ij} represent the bond order, i.e. the strength of the bonds, which depends inversely on the number of bonds, the bond angles (θ_{ijk}) and optionally the relative bonds lengths (r_{ij}, r_{jk}). Notice that an additional cut-off term a_{ij} was originally multiplied to f_R as a way of including terms that limit the range of the interactions to the first neighbour shell. These kind of limitations is already included in b_{ij} for the attractive term f_A but is often omitted for the repulsive term f_R , and we do so to by setting $a_{ij} = 1$.

The cut-off function f_C goes from 1 to 0 over a small interval range $R \pm D$ as

$$f_C(r) = \begin{cases} 1 & r < R - D \\ \frac{1}{2} - \frac{1}{2} \sin\left(\frac{\pi}{2} \frac{r-R}{D}\right) & R - D < r < R + D \\ 0 & r > R + D \end{cases},$$

which is continuous and differentiable for all r . R is usually chosen to include only the first neighbour shell. The repulsive and attractive terms f_R and f_A is modelled as an exponential function, similar to a morse potential,

$$f_R(r) = A \exp(-\lambda_1 r),$$

$$f_A(r) = -B \exp(-\lambda_2 r).$$

The novel feature of the model lies in modeling of the bond order b_{ij} which includes three-body interactions by summing over a third atom $k \neq i, j$ within the cut-off $r_{ik} < R + D$ as shown in the following.

$$b_{ij} = (1 + \beta^n \zeta_{ij}^n)^{-\frac{1}{2n}} \quad (1.6)$$

$$\zeta_{ij} = \sum_{k \neq i, j} f_C(r_{ik}) g\left(\theta_{ijk}(r_{ij}, r_{ik})\right) \exp(\lambda_3 m (r_{ij} - r_{ik})^m) \quad (1.7)$$

$$g(\theta) = \gamma_{ijk} \left(1 + \frac{c^2}{d^2} - \frac{c^2}{[d^2 + (\cos \theta - \cos \theta_0)^2]} \right). \quad (1.8)$$

In eq. (1.8) $\zeta_{i,j}$ is an effective coordination and $g(\theta)$ captures angle dependency as it is minimized at the equilibrium angle $\theta = \theta_0$.

The parameters used to model the graphene C-C bonds is summarized in table 1.3

Table 1.3: Parameters for the tersoff potential used for intermolecular interactions in the graphene sheet

Parameter	Value	Description
m	3.0	Default (not used since $\lambda_3 = 0$)
γ	1.0	...
λ_3	0.0 \AA^{-1}	...
c	3.8049×10^4	Strength of the angular effect
d	4.3484	Determines the “sharpness” of the angular dependency
$\cos(\theta_0)$	-0.57058	Cosine of the equilibrium angle
n	0.72751	Power law exponent for the bond order dependency
β	1.5724×10^{-7}	...
λ_2	2.2119 \AA^{-1}	Decay of repulsion potential term
B	346.74 eV	Attractive potential term minimum at core ($r_{ij} = 0$).
R	1.95 Å	Center distance for cut-off
D	0.15 Å	Thickness of cut-off layers
λ_1	3.4879 \AA^{-1}	Decay of repulsion potential term
A	1393.6 eV	Repulsion potential term at core ($r_{ij} = 0$)

1.2.2 Integration

Having defined a system of particles governed by interatomic potentials we need to move the system forward in time. By solving Newtons equations of motion we effectively do so by sampling the microcanonical ensemble characterized by a constant number of particles N , volume V and energy E , hence denoted NVE. Newtons equaitons of motion read

$$m_i \frac{d^2 \mathbf{r}_i}{dt^2} = \mathbf{F}_i = -\nabla U_i \quad (1.9)$$

where i is the particle index and m_i its mass, $\mathbf{r}_i = (x_i, y_i, z_i)$ the position, t is time, $\nabla_i = (\frac{\partial}{\partial x_i}, \frac{\partial}{\partial y_i}, \frac{\partial}{\partial z_i})$ and U_i the potential energy. In system the potential energy is a function of the particle positions of nearby particles depending on the specefic potential in use. Since the forces defined by the potentials is conservative we expect the energy of the solution to be conserved. We redefine eq. (1.9) in terms of two coupled first order differential equations

$$\dot{\mathbf{v}}_i(t) = \frac{\mathbf{F}}{m_i}, \quad \dot{\mathbf{r}}_i(t) = \mathbf{v}_i(t), \quad (1.10)$$

where $\dot{x} = dx/dt$ (Newton's notation) and $\mathbf{v} = (v_x, v_y, v_z)$ is velocity. Numerically we can solve the coupled equations (eq .(1.10)) by integrating over discrete timnesteps. That is, we discretize the solution into temporal steps $t_k = t_0 + k \cdot \Delta t$ with time-step Δt .

1.2.2.1 Velocity Verlet

A common algorithm to integrate Newtons equation of motion (as formulated in eq. (1.10)) is the *velocity verlet*. We can derive the algorithm by the use of Taylor expansions. We begin by expanding the next-step position vector $\mathbf{r}_i(t + \Delta t)$ at time t

$$\mathbf{r}_i(t + \Delta t) = \mathbf{r}_i(t) + \dot{\mathbf{r}}_i(t)\Delta t + \frac{\ddot{\mathbf{r}}_i(t)}{2}\Delta t^2 + \mathcal{O}(\Delta t^3), \quad (1.11)$$

where $\ddot{\mathbf{r}} = d^2\mathbf{r}/dt^2$ and Δt^n is simply the relaxed notation for $(\Delta t)^n$. Similar we take the expansions of the next-step velocity vector $\mathbf{v}_i(t + \Delta t)$ at time t

$$\mathbf{v}_i(t + \Delta t) = \mathbf{v}_i(t) + \dot{\mathbf{v}}_i(t)\Delta t + \frac{\ddot{\mathbf{v}}_i(t)}{2}\Delta t^2 + \mathcal{O}(\Delta t^3). \quad (1.12)$$

Finally, by taking the expansion of $\dot{\mathbf{v}}_i(t + \Delta t)$ we can eliminate the $\ddot{\mathbf{v}}_i$ -term in eq. (1.12) and simplify it as shown in the following.

$$\begin{aligned}
\dot{\mathbf{v}}_i(t + \Delta t) &= \dot{\mathbf{v}}_i(t) + \ddot{\mathbf{v}}_i(t)\Delta t + \mathcal{O}(\Delta t^2) \\
\frac{\ddot{\mathbf{v}}_i(t)}{2}\Delta t^2 &= \frac{\Delta t}{2}(\dot{\mathbf{v}}(t + \Delta t) - \dot{\mathbf{v}}_i(t)) + \mathcal{O}(\Delta t^3) \\
&\Downarrow \\
\mathbf{v}_i(t + \Delta t) &= \mathbf{v}_i(t) + \dot{\mathbf{v}}_i(t)\Delta t + \frac{\Delta t}{2}(\dot{\mathbf{v}}_i(t + \Delta t) - \dot{\mathbf{v}}_i(t)) + \mathcal{O}(\Delta t^3) \\
&= \mathbf{v}_i(t) + \frac{\Delta t}{2}(\dot{\mathbf{v}}_i(t) + \dot{\mathbf{v}}_i(t + \Delta t)) + \mathcal{O}(\Delta t^3).
\end{aligned} \tag{1.13}$$

By combining eq. (1.11) and eq. (1.13) and using Newton's second equation $\dot{\mathbf{v}} = \mathbf{F}_i(t)/m_i$ and $\mathbf{v} = \dot{\mathbf{r}}$ we arrive at the final scheme

$$\begin{aligned}
\mathbf{r}_i(t + \Delta t) &= \mathbf{r}_i(t) + \mathbf{v}_i(t)\Delta t + \frac{\mathbf{F}_i(t)}{2m_i}\Delta t^2 + \mathcal{O}(\Delta t^3), \\
\mathbf{v}_i(t + \Delta t) &= \mathbf{v}_i(t) + \frac{\mathbf{F}_i(t) + \mathbf{F}_i(t + \Delta t)}{2m_i}\Delta t + \mathcal{O}(\Delta t^3).
\end{aligned}$$

The scheme will give a local error of order Δt^3 corresponding to a global error of Δt^2 . One of the most popular ways to implement this numerically is as stated in the following steps.

1. Calculate $v_{k+\frac{1}{2}} = v_k + \frac{F_k}{2m}\Delta t$.
2. Calculate $r_{k+1} = r_k + v_{k+\frac{1}{2}}\Delta t$.
3. Evaluate the force $F_{k+1} = F(r_{k+1})$.
4. Calculate $v_{k+1} = v_{k+\frac{1}{2}} + \frac{F_{k+1}}{2m}\Delta t$

1.2.3 Thermostats

As we already mentioned above in Sec. 2, any kind of sliding friction involves mechanical work, some of which is then transformed into heat (the rest going into structural transformations, wear, etc.). The heat is then transported away by phonons (and electrons in the case of metallic sliders) and eventually dissipated to the environment [3].

Likewise all excitations generated in the simulations should be allowed to propagate in the system and disperse in the bulk of both sheet and substrate. Due to small simulation size this is likely to reflect back and ‘pile up’ unphysically. Thus in order to avoid continuous heating and attain a steady state the (Joule) heat must be removed at a steady state. This is very the viscous damping of the Langevin equations enter the picture. It can be difficult to set the value γ for the magnitude of this damping. The unphysical introduction of heat sink can be mitigated by some modifications he mention, which is kind of next level I guess.

1.2.3.1 Langevin thermostat

In order to control the temperature of the system we introduce the so-called Langevin thermostat. This is a stochastic thermostat that modifies Newton's equation of motion such that solution lies in the canonical ensemble characterized by a constant number of particles N , constant volume V and constant temperature T , hence denoted NVT. The canonical ensemble system is represented by the finite system being in contact with an infinite heat bath of temperature T . The NVT ensemble is equivalent to sampling a system in thermodynamic equilibrium where the weight of each microscopic state is given by the Boltzmann factor $\exp[-E/(k_B T)]$.

The Langevin equation is the modified version of Newton's second law for a Brownian particle. A Brownian particle is a small particle suspended in liquid, e.g. pollen or dust, named after Robert Brown (1773–1858) who was the first to observe its jittery motion. The Langevin equation describes this motion as the combination

of viscous drag force $-\gamma\mathbf{v}$, where γ is a positive friction coefficient and \mathbf{v} the velocity vector, and a random fluctuation force \mathbf{R} . The langevin equation reads

$$m \frac{d\mathbf{v}}{dt} = -\gamma\mathbf{v} + \mathbf{R} \quad (1.14)$$

where m is the particle mass. This effectively describes the particle of interest, the brownian particle, as being suspendend in a sea of smaller particles. The collision with these smaller particles is modelled by the drag force and the fluctuation force. We notice that if the fluctuation force is excluded eq. (1.14) becomes

$$m \frac{d\mathbf{v}}{dt} = -\gamma\mathbf{v} \Rightarrow \mathbf{v}_i(t) = v(0)e^{-\frac{\gamma t}{m}},$$

where the solution shows that the brownian particle will come to a complete stop after a long time $\mathbf{v}_i(t \rightarrow \infty) \rightarrow \mathbf{0}$. This is in violation with the equipartition theorem

$$\frac{1}{2}m\langle v^2 \rangle_{eq} = \frac{k_B T}{2},$$

and hence the fluctuation force is nessecary to obtain the correct equilibrium.

The following calculations are done in one dimension in order to simplify the notation. We describe the statistical nature of the collisions as a sum of independent momentum transfers

$$\Delta P = \sum_i^N \delta p_i$$

where ΔP denotes the change of momentum after N momentum transfers δp_i from the environment to the brownian particle. We assume the first and second moments $\langle \delta p \rangle = 0$ and $\langle \delta p^2 \rangle = \sigma^2$. When N is large the central limit theorem states that the random variable ΔP has a gaussian distribution with $\langle P \rangle = 0$ and $\langle \Delta P^2 \rangle = N\sigma^2$. If we consider the momentum change ΔP over a discrete time Δt , where the number of collisiosn is proportional to time $N \propto \Delta t$, the corresponding fluctuation force $R = \Delta P/\Delta t$ will have a variance

$$\langle R^2 \rangle = \frac{\langle \Delta P^2 \rangle}{\Delta t^2} = \frac{N\sigma^2}{\Delta t^2} \propto \frac{1}{\Delta t}.$$

In a computer simulation we need to pick a random force $R(t)$ from a Gaussian distribution every time-step Δt . These forces will not be correlated as long as Δt is larger than the correlation time of the forces from the molecules which we will assume for this model (I think there exist corrections for this to refer to here). With this assumption we can write the correlation function as

$$\langle R(t)R(0) \rangle = \begin{cases} \frac{a}{\Delta t}, & |\Delta t| < \Delta t/2 \\ 0, & |\Delta t| > \Delta t/2, \end{cases} \quad (1.15)$$

where a is some strength of (...?). In the limit $\Delta t \rightarrow 0$ the correlation function becomes

$$\langle R(t)R(0) \rangle = a\delta(t), \quad (1.16)$$

where δ denotes the dirac delta function. This is valid for all spatial coordinates which will all be independent of each other. Since both the drag force and the fluctuation force originate from the molecular fluid, where the drag force $-\alpha\mathbf{v}$ is velocity dependent it is reasonable to assume that fluctuation force is independent of velocity, i.e. $\langle R_i v_j \rangle = 0$ for all cartesian indices i and j .

In the following we will attempt justify the Langevin equaiton (why it is like it is) and determine the relationship between the drag coefficient γ and the random force R .

From the Langevin equation eq. (1.14) we can compute the velocity autocorrelation function (Move to appendix?). We do this in one dimension for simplicity. We begin by multiplying by $(e^{\gamma t/m})/m$

$$\dot{v}(t)e^{\gamma t/m} + \frac{\gamma}{m}v(t)e^{\gamma t/m} = \frac{F}{m}e^{\gamma t/m},$$

and integrate from $t = -\infty$. By the use of integration by parts on the latter term on the left hand side we calculate the velocity

$$\begin{aligned} \int_{-\infty}^t dt' \dot{v}(t') e^{\frac{\gamma t'}{m}} + \frac{\gamma}{m} v(t) e^{\frac{\gamma t}{m}} &= \int_{-\infty}^t dt' e^{\frac{\gamma t'}{m}} \frac{F(t')}{m} \\ \int_{-\infty}^t dt' \dot{v}(t') e^{\frac{\gamma t'}{m}} + \left(\left[v(t') e^{\frac{\gamma t'}{m}} \right]_{-\infty}^t - \int_{-\infty}^t dt' \dot{v}(t') e^{\frac{\gamma t'}{m}} \right) &= \int_{-\infty}^t dt' e^{\frac{\gamma t'}{m}} \frac{F(t')}{m} \\ v(t) &= \int_{-\infty}^t dt' e^{\frac{-\gamma(t-t')}{m}} \frac{F(t')}{m}, \end{aligned}$$

where $e^{\frac{-\gamma t}{m}}$ plays the role of a response function. We can then calculate the autocorrelation

$$\begin{aligned} \langle v(t)v(0) \rangle &= \int_{-\infty}^t dt_1 \int_{-\infty}^0 dt_2 e^{\frac{t-t_1-t_2}{m}} \frac{\langle F(t_1)F(t_2) \rangle}{m^2} \\ &= \int_{-\infty}^t dt_1 \int_{-\infty}^0 dt_2 e^{\frac{t-t_1-t_2}{m}} \frac{a\delta(t_1-t_2)}{m^2} \\ &= \int_{-\infty}^0 dt_2 e^{\frac{t-2t_2}{m}} \frac{a}{m^2} = \frac{a}{2m\gamma} e^{-\frac{\gamma t}{m}}, \end{aligned}$$

where we used eq. (1.16) and the fact that the integration commutes with the average (we are allowed to flip the order). By comparing this with the equipartition theorem we get

$$\begin{aligned} \frac{1}{2}m\langle v^2 \rangle &= \frac{k_B T}{2} \\ \frac{1}{2}m\langle v(0)v(0) \rangle &= \frac{a}{4\gamma} = \frac{k_B T}{2} \\ a &= 2\gamma k_B T \end{aligned}$$

We notice the appearance of γ meaning that the magnitude of the fluctuations increase both with friction and temperature. Further we can integrate the velocity over time to get displacement $x(t)$ and show that the variance (show this? In appendix maybe?) is

$$\langle x^2(t) \rangle = \frac{2k_B T}{\gamma} \left(t - \frac{m}{\gamma} \left(1 - e^{-\gamma t/m} \right) \right),$$

where for $t \gg m/\gamma$ only the t -term survives yielding

$$\langle x^2(t) \rangle = 2k_B T t / \gamma.$$

In 1D, the diffusion constant D is related to the variance as $\langle x^2 \rangle = 2Dt$, meaning that this represents the einstein relation $D = \mu k_B T$ with the mobility $\mu = 1/\gamma$.

when $t \ll m/\gamma$ we use the Taylor expansion $1 - e^{-x} \approx x - x^2/2$ for $x \ll 1$ to get

$$\langle x^2(t) \rangle = \frac{k_B T}{m} t^2$$

which exactly matches the thermal velocity

$$v_{\text{th}} \frac{\langle x^2(t) \rangle}{t^2} = \frac{k_B T}{m}$$

which follows from the equipartition theorem. The finite correlation time γ/m hence describe the crossover from the ballistic regime $\sqrt{\langle x^2(t) \rangle} \propto t$ to the diffusive regime $\sqrt{\langle x^2(t) \rangle} \propto \sqrt{t}$.

Introduce the fluctuation-dissipation theorem concept earlier since this is a motivation for the Langevin equation.

1.2.3.2 Implementing Langevin

The implementation of the Langevin equation into LAMMPS follows [35] and updates the force vector for each particle as

$$\begin{aligned}\mathbf{F} &= \mathbf{F}_c + \mathbf{F}_f + \mathbf{F}_r \\ &= -\nabla U - \gamma m \mathbf{v} + \sqrt{\frac{2k_B T m \gamma}{\Delta t}} \mathbf{h}(t)\end{aligned}\quad (1.17)$$

where \mathbf{F}_c is the conservative force computed via the usual inter-particle interactions described by the potential U , \mathbf{F}_f is the drag force and \mathbf{F}_r is the random fluctuation force where \mathbf{h} is a random vector drawn from a normal distribution with zero mean and unit variance. Notice that this generalized description of the Langevin equation deviates from the presentation in eq. (1.14) since we have added the conservative force \mathbf{F}_c , but also by the appearance of the mass in both the drag force and the fluctuation force due to the introduction of damping. It is beyond our scope to comprehend this. However, the fact that Δt now appears in the denominator for the random force variance $2k_B T m \gamma / \Delta t$ is due to the fact that we have discretized time. This is in agreement with the formulation in eq. (1.15). By applying eq. (1.17) we get the refined velocity verlet scheme

$$\begin{aligned}\mathbf{v}_i(t + \Delta t/2) &= \mathbf{v}_i(t) - \frac{\Delta t}{2} \left(\frac{\nabla_i U(t)}{m_i} + \gamma \mathbf{v}_i \right) + \sqrt{\frac{k_B T \gamma \Delta t}{2m_i}} \mathbf{h}_i \\ \mathbf{r}_i(t + \Delta t) &= \mathbf{r}_i(t) + \mathbf{v}_i(t + \Delta t/2) \Delta t \\ \mathbf{v}_i(t + \Delta t) &= \mathbf{v}_i(t + \Delta t/2) - \frac{\Delta t}{2} \left(\frac{\nabla_i U(t + \Delta t)}{m_i} + \gamma \mathbf{v}_i(t + \Delta t/2) \right) + \sqrt{\frac{k_B T \gamma \Delta t}{2m_i}} \mathbf{h}_i\end{aligned}$$

with new random vector \mathbf{h}_i for each particle and each update. Notice however, that LAMMPS only apply this scheme to the particle groups with the thermostat on.

1.2.4 MD limitations (?)

1.2.5 LAMMPS

1.3 Defining the system

The simulated system consists of two major parts: A 2D graphene sheet and a 3D Silicon “bulk” substrate. These parts interact with a van der Waals force (modelled by the LJ potential). We apply a normal load to the sheet inducing a normal force response between the sheet and substrate. By dragging the sheet along the substrate we measure the responding frictional forces.

1.3.1 Region definitions (Sheet, pullblocks and substrate)

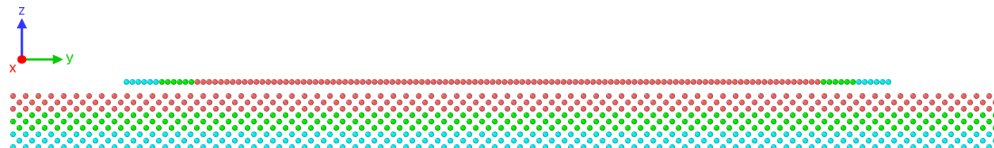
The system, sheet and substrate, is further subdivided according to functionality in the MD simulations. The sheet ends are reserved for so-called *pull blocks*, which is used for application of normal load, stretching and dragging the sheet, and as a thermostat, while the remaining *inner sheet* is left as an untouched (NVE) canvas for kirigami cuts. The pull blocks are equally split between a thermostat part and a rigid part which is locked into a single rigid body after an initial relaxation period. Note that the rigid part of the pull blocks on both sides is considered a single rigid object even though they are physically separated. This means that all force interactions on these parts will be applied as a common average making the move in total synchronization. The substrate is equally divided into three parts: The *upper layers* (NVE) responsible for the sheet-substrate interaction, the *middle layers* being a thermostat (NVT), and the *bottom layers* is frozen (rigid and fixed) in the initial lattice structure to ensure that the substrate stays in place. In figure 1.8 the system is displayed with colors matching the three distinct roles:

1. Red: NVE parts which govern the frictional behaviour of interest.

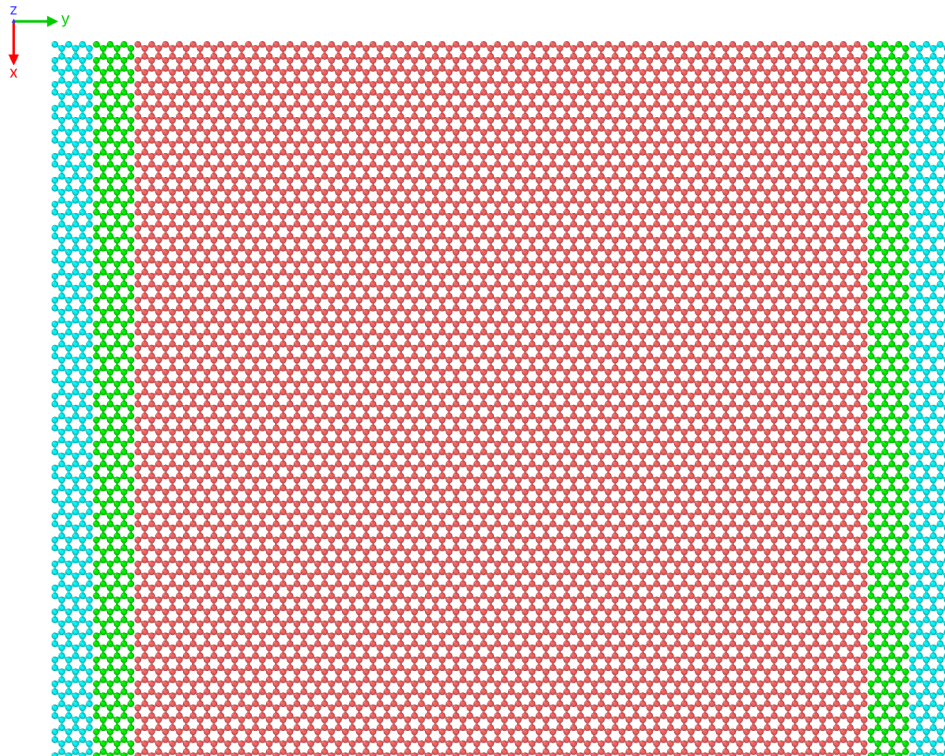
2. Green: Thermostats (NVT) surrounding the NVE parts in order to modify the temperature without making disturbing changes to the interaction of the sheet and substrate.
3. Blue: Parts that is initially or eventually turned in to rigid objects. For the substrate this is additionally locked off and immobile.

The total system size in terms of atom count is given in table 1.4 while the sheet length dimension is given in table ??

The total system size (without cuts in the sheet) is 27456 atoms, and the distribution into the various regions is shown in table 1.4. The length dimensions of the sheet is given in table 1.5.



(a) Side view showing sheet on top of the substrate.



(b) Top view showing only the sheet.

Figure 1.8: System configuration colorized to indicate NVE parts (red), thermostat parts (green) and rigid parts (blue).

Table 1.4: Amount of atoms in the various system regions in the case of no cutting applied to the sheet.

Region	Total	Sub region	Sub total	NVE	NVT	Rigid
Sheet	7800	Inner sheet	6360	6360	0	0
		Pull blocks	1440	0	720	720
Substrate	19656	Upper	6552	6552	0	0
		Middle	6552	0	6552	0
		Bottom	6552	0	0	6552
All	27456			12912	7272	7272

Table 1.5: Sheet dimensions comparing the full sheet to its subdivisions: inner sheet and pull blocks.

Group	x, y -dim	dim [Å]	Area [Å ²]
Full sheet	$x_S \times y_S$	130.029 × 163.219 Å	21,223.203
Inner sheet	$x_S \times 81.40 \%_{y_s}$	130.029 × 132.853 Å	17,274.743
Pull blocks	$2 \times x_S \times 9.30 \%_{y_s}$	2 × 130.029 × 15.183 Å	2 × 1,974.230

1.3.2 Numerical procedure

The numerical procedure for the friction simulations can be arranged as the following.

1. Relax (15 ps): The sheet and substrate is relaxed for 15 ps. They are both initially added in their crystalline form. The sheet is constrained under three hard spring forces (spring constant 10^5 eV/Å² $\sim 1.6 \times 10^6$ N/m): One spring attaches the sheet center of mass (CM) to its original position preventing drift, while the remaining two are attached to the CM for the pull blocks to their initial position respectively to prevent rotation. These spring forces are immediately terminated after the relax phase. In this phase the pull blocks are only rigid with respect to the z-direction (perpendicular to the sheet). That is, all the forces in the z-direction are summed up and distributed on the pull blocks while it is free to expand and contract in the x-y-plane. This is mainly to ensure that it achieves the correct lattice spacing according to the temperature of the system. For the remaining phases the rigid parts of the pull block is in fact rigid with respect to all directions.
2. Stretch: The sheet is stretched by separating the rigid parts of the pullblock at constant velocity until the desired stretch amount is met.
3. Pause 1 (5 ps): The sheet is relaxed for 5 ps after the stretch procedure.
4. Pause 2 (Normal load): The normal load is applied to the rigid parts of the pull blocks together with a damping force to prevent hard impact between sheet and substrate as the separating distance is now reduced depending on the strength of the normal load. The damper is terminated after 0.5 ps, as this was suitable for the extreme load cases of our force range, and the system is relaxed until a total of 5 ps has passed.
5. Drag: A virtual atom is introduced into the simulation which exclusively interacts with the rigid parts of the pull through a spring force with variable spring constant K in the x-y-plane. The z-direction is not affected by the spring force and is governed by the balance between normal load and the normal force response from the sheet-substrate interaction. The virtual atom is immediately given a constant velocity corresponding to a variable *drag speed* parameter

At the initial timestep the three nearest neighbours (at distance 1.42 Å) of all graphene atoms are recorded. If these nearest neighbours exceed a threshold of 4 Å this raises a rupture flag which halts the simulation early. Thus, we effectively prevent any kind of wear on the sheet. For the substrate we do not perform such an analysis but only visually confirms that no wear is occurring under the most extreme simulation parameters.

1.3.3 Creating the sheet

We are going to create a 2D sheet graphene sheet.

1.3.3.1 Graphene

Graphene is a single layer of carbon atom, graphite is the bulk, arranged in a hexagonal lattice structure. We can describe the 2D crystal structure in terms of its primitive lattice vector and a basis. That is we populate each lattice site by the given basis and translate it to fill the whole plane by any linear combination of the lattice vectors

$$\mathbf{T}_{mn} = m\mathbf{a}_1 + n\mathbf{a}_2, \quad m, n \in \mathbb{N}.$$

For graphene we have the primitive lattice vectors

$$\mathbf{a}_1 = a \left(\frac{\sqrt{3}}{2}, -\frac{1}{2} \right), \quad \mathbf{a}_2 = a \left(\frac{\sqrt{3}}{2}, \frac{1}{2} \right), \quad |\mathbf{a}_1| = |\mathbf{a}_2| = 2.46 \text{ \AA}.$$

Notice that we deliberately excluded the third coordinate as we only consider a single graphene layer on not the bulk graphite consisting of multiple layers stacked on top of each other. The basis is

$$\left\{ (0,0), \frac{a}{2} \left(\frac{1}{\sqrt{3}}, 1 \right) \right\}$$

It turns out that the spacing between atoms is equal for all pairs with an interatomic distance

$$\left| \frac{a}{2} \left(\frac{1}{\sqrt{3}}, 1 \right) \right| \approx 1.42 \text{ \AA}.$$

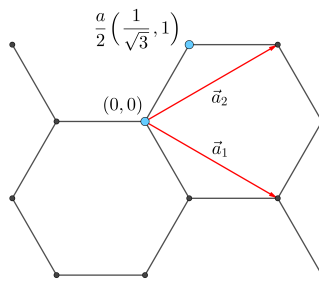


Figure 1.9: Graphene crystal structure with basis.

1.3.3.2 Indexing

In order to define the cut patterns applied to the graphene sheet we must define an indexing system. We must ensure that this gives an unique description of the atoms as we eventually want to pass a binary matrix, containing 0 for removed atom and 1 for present atom, that uniquely describes the sheet. We do this by letting the x-coordinate point to zigzag chains and the y-coordinate to the position along that chain. This is illustrated in figure 1.10. Other solutions might naturally involve the lattice vectors, but as these only can be used to translate to similar basis atoms a unfortunate duality is introduced as ones need to include the basis atom of choice into the indexing system. With the current system we notice that locality is somewhat preserved. That is, atom (i, j) is in the proximity of $\{(i+1, j), (i-1, j), (i, j+1), (i, j-1)\}$, but only three of them is categorized as nearest neighbours due to the hexagonal structure of the lattice. While $(i, j \pm 1)$ is always nearest neighbours the

neighbour in the x-direction flip sides with incrementing y-coordinate. That is the nearest neighbours (NN) is decided as

$$\begin{aligned} j \text{ is even} &\rightarrow \text{NN} = \{(i+1, j), (i, j+1), (i, j-1)\}, \\ j \text{ is odd} &\rightarrow \text{NN} = \{(i-1, j), (i, j+1), (i, j-1)\}. \end{aligned}$$

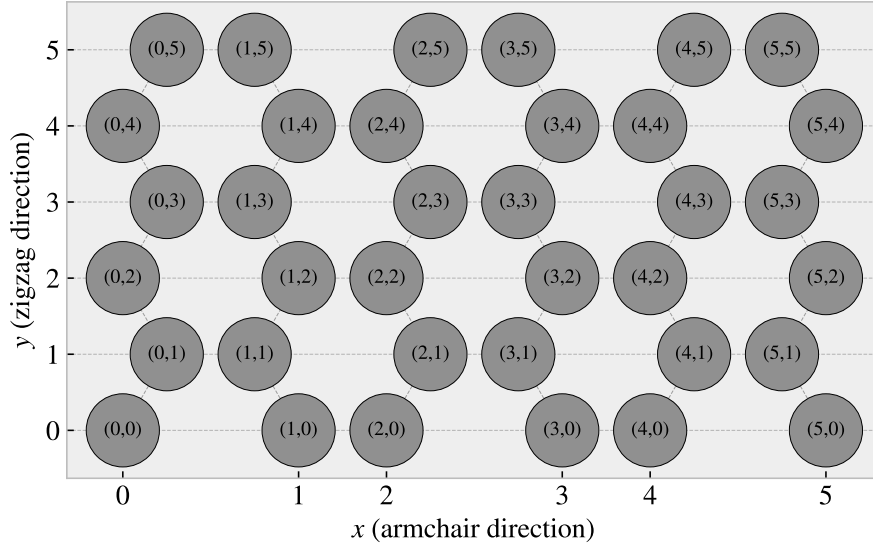


Figure 1.10: Graphene atom indexing

1.3.3.3 Removing atoms

As a mean to ease the formulation of cut patterns we introduce pseudo center element in each gap of the hexagonal honeycombs, see figure 1.11.

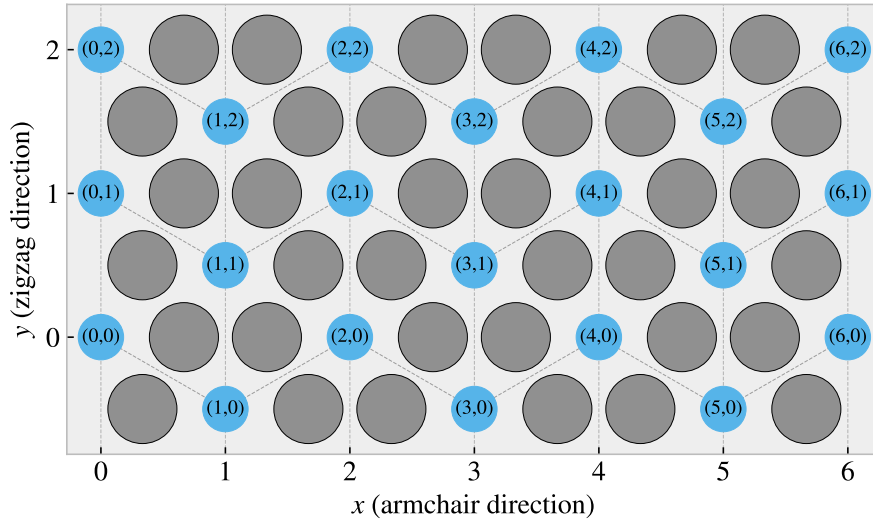


Figure 1.11: Graphene center indexing

Similar to the case of the indexing for the carbon atoms themself the nearest neighbour center elements alternate with position, this time along the x-coordinate. Each center element has six nearest neighbours, in clock wise direction we can denote them: “up”, “upper right”, “lower right”, “down”, “lower left”, “upper left”.

The “up” and “down” is always accessed as $(i, j \pm 1)$, but for even i the $(i + 1, j)$ index corresponds to the “lower right” neighbour while for odd i this corresponds to the “upper right” neighbour. This shifting applies for all left or right neighbours and the full neighbour list is illustrated in figure 1.12.

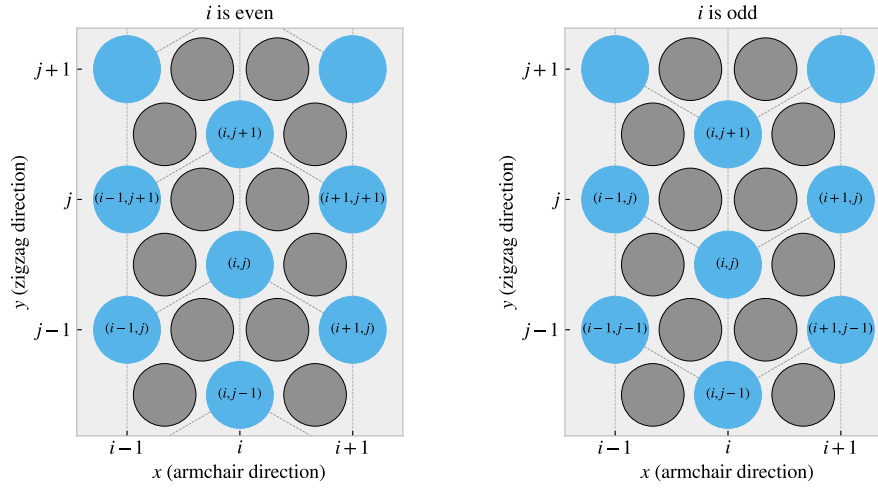


Figure 1.12: Graphene center elements directions

We define a cut pattern by connecting center elements into connected paths. As we walk element to element we remove atoms according to one of two rules

1. Remove intersection atoms: We remove the pair of atoms placed directly in the path we are walking. That is, when jumping to the “up” center element we remove the two upper atoms located in the local hexagon of atoms. This method is sensitive to the order of the center elements in the path.
2. Remove all surrounding atoms: We simply remove all atoms in the local hexagon surrounding each center element. This method is independent of the ordering of center elements in the path.

We notice that removing atoms using either of these rules will not guarantee an unique cut pattern. Rule 1 is the more sensitive to paths but we realize that, for an even i , we will remove the same five atoms following either of the following paths.

$$\begin{aligned} (i, j) &\rightarrow \underbrace{(i + 1, j + 1)}_{\text{upper right}} \rightarrow \underbrace{(i, j + 1)}_{\text{up}} \rightarrow \underbrace{(i + 1, j + 2)}_{\text{uppright + up}} \rightarrow \underbrace{(i + 1, j + 1)}_{\text{upper right}} \\ (i, j) &\rightarrow \underbrace{(i + 1, j + 1)}_{\text{upper right}} \rightarrow \underbrace{(i + 1, j + 2)}_{\text{uppright + up}} \rightarrow \underbrace{(i, j + 1)}_{\text{up}} \end{aligned}$$

For rule 2 it is even more obvious that different paths can result in the same atoms being removed. This is the reason that we needed to define and indexing system for the atom position itself even though that all cuts generated manually will use the center element path as reference.

Illustrate some delete path?

1.3.4 Kirigami patterns

1.3.4.1 Pop-up

1.3.4.2 Honeycomb

1.3.4.3 Random walk

1.4 Pressure reference

Find place to put this.

In order to relate the magnitude of the normal force in our friciton measurement we will use the pressure as a reference. We will use the pressure underneath a stiletto shoe as a worst case for human pressure execution underneath the shoes. From (source 1) it is reported that the diameter of a stiletto heeled shoe can be less than 1 cm. Hence a 80 kg man³ standing on one stiletto heels (with all the weight on the heel) will result in a pressure corresponding diameter of

$$P = \frac{F}{A} = \frac{mg}{r^2\pi} = \frac{80 \text{ kg} \cdot 9.8 \frac{\text{m}}{\text{s}^2}}{(\frac{1 \times 10^{-2} \text{ m}}{2})^2\pi} = 9.98 \text{ MPa}$$

While this is in itself a spectacular realization that is often used in introduction physics courses (source 2) to demonstrate the rather extreme pressure under a stiletto heel (greater than the foot of an elephant) (how many Atmos) this serves as a reasonable upperbound for human executed pressure. With a full sheet area of $\sim 21 \times 10^3 \text{ Å}^2$ we can achieve a similar pressure of $\sim 10 \text{ MPa}$ with a normal force

$$F_N = 10 \text{ MPa} \cdot 21 \times 10^{-17} \text{ m}^2 = 2.10 \text{ nN}$$

Of course this pressure might be insufficient for various industrial purposes, but with no specific procedure in mind this serves as a decent reference point. Notice that if we consider a human foot with area 113 cm^2 the pressure drops to a mere 70 kPa corresponding to $\sim 0.01 \text{ nN}$.

1.5 Fourier Transform (light)

Find out where to put this if necessary.

Fourier transform is a technique where we transform a function $f(t)$ of time to a function $F(k)$ of frequency. The Forward Fourier Transform is done as

$$F(k) = \int_{-\infty}^{\infty} f(t)e^{-2\pi i k x} dt$$

For any complex function $F(k)$ we can decompose it into magnitude $A(k)$ and phase $\phi(k)$

$$F(k) = A(k)e^{i\phi(k)}$$

Hence when performing a Forward Fourier transform on a time series we can determine the amplitude and phase as a function of frequency as

$$A(k) = |F(k)|^2, \quad \phi(k) = \Im \ln F(k)$$

- Real life procedures to mimic in computation, for instance Atomic Force Microscopy (AFM) for friction measurements.
- Available technology for test of my findings if successful (possibilities for making the nano machine)

1.6 Machine Learning (ML)

- Feed forward fully connected
- CNN
- GAN (encoder + decoder)
- Genetic algorithm

³Yes, a man can certainly wear stiletto heals.

- Using machine learning for inverse designs partly eliminate the black box problem. When a design is produced we can test it, and if it works we not rely on machine learning connections to verify it's relevance.
- However, using explanations techniques such as maybe t-SNE, Deep dream, LRP, Shapley values and linearizations, we can try to understand why the AI chose as it did. This can lead to an increased understanding of each design feature. Again this is not dependent on the complex network of the network as this can be tested and verified independently of the network.

1.6.1 Feed forward network / Neural networks

1.6.2 CNN for image recognition

1.6.3 GAN (encoder + decoder)

1.6.4 Inverse designing using machine learning

1.6.5 Prediction explanation

1.6.5.1 Shapley

1.6.5.2 Linearizations

1.6.5.3 LRP

1.6.5.4 t-SNE

Bibliography

- [1] E. Gnecco and E. Meyer, *Elements of Friction Theory and Nanotribology*. Cambridge University Press, 2015, [10.1017/CBO9780511795039](https://doi.org/10.1017/CBO9780511795039).
- [2] H.-J. Kim and D.-E. Kim, *Nano-scale friction: A review*, .
- [3] N. Manini, O. M. Braun, E. Tosatti, R. Guerra and A. Vanossi, *Friction and nonlinear dynamics*, *Journal of Physics: Condensed Matter* **28** (jun, 2016) 293001.
- [4] Bhushan, *Introduction*, ch. 1, pp. 1–?. John Wiley & Sons, Ltd, 2013.
<https://onlinelibrary.wiley.com/doi/pdf/10.1002/9781118403259.ch1>.
<https://doi.org/10.1002/9781118403259.ch1>.
- [5] B. Bhushan and A. V. Kulkarni, *Effect of normal load on microscale friction measurements*, *Thin Solid Films* **278** (1996) 49–56.
- [6] J. H. Dieterich, *Time-dependent friction in rocks*, *Journal of Geophysical Research (1896-1977)* **77** (1972) 3690–3697, [<https://agupubs.onlinelibrary.wiley.com/doi/pdf/10.1029/JB077i020p03690>].
- [7] Y. Mo, K. T. Turner and I. Szlufarska, *Friction laws at the nanoscale*, .
- [8] W. Commons, *File:asperities.svg — wikimedia commons, the free media repository*, 2022.
- [9] G. Carbone and F. Bottiglione, *Asperity contact theories: Do they predict linearity between contact area and load?*, *Journal of the Mechanics and Physics of Solids* **56** (2008) 2555–2572.
- [10] J. A. Greenwood and J. B. P. Williamson, *Contact of nominally flat surfaces*, Dec, 1966. [10.1098/rspa.1966.0242](https://doi.org/10.1098/rspa.1966.0242).
- [11] B. N. J. Persson, *Theory of rubber friction and contact mechanics*, *The Journal of Chemical Physics* **115** (2001) 3840–3861, [<https://doi.org/10.1063/1.1388626>].
- [12] B. Luan and M. O. Robbins, *The breakdown of continuum models for mechanical contacts*, .
- [13] J. Norell, A. Fasolino and A. Wijn, *Emergent friction in two-dimensional frenkel-kontorova models*, *Physical Review E* **94** (04, 2016) .
- [14] M. Dienwiebel, N. Pradeep, G. S. Verhoeven, H. W. Zandbergen and J. W. Frenken, *Model experiments of superlubricity of graphite*, *Surface Science* **576** (2005) 197–211.
- [15] J. A. van den Ende, A. S. de Wijn and A. Fasolino, *The effect of temperature and velocity on superlubricity*, *Journal of Physics: Condensed Matter* **24** (oct, 2012) 445009.
- [16] X. Zhao, M. Hamilton, W. G. Sawyer and S. S. Perry, *Thermally activated friction*, .
- [17] S. Y. Krylov, K. B. Jinesh, H. Valk, M. Dienwiebel and J. W. M. Frenken, *Thermally induced suppression of friction at the atomic scale*, *Phys. Rev. E* **71** (Jun, 2005) 065101.
- [18] B. Bhushan, *Nanotribology and nanomechanics*, *Wear* **259** (2005) 1–?
- [19] P. Zhu and R. Li, *Study of nanoscale friction behaviors of graphene on gold substrates using molecular dynamics*, .
- [20] J. Zhang, E. Osloub, F. Siddiqui, W. Zhang, T. Ragab and C. Basaran, *Anisotropy of graphene nanoflake diamond interface frictional properties*, *Materials* **12** (2019) .
- [21] F. Bonelli, N. Manini, E. Cadelano and L. Colombo, *Atomistic simulations of the sliding friction of graphene flakes*, .
- [22] X. Feng, S. Kwon, J. Y. Park and M. Salmeron, *Superlubric sliding of graphene nanoflakes on graphene*, .
- [23] M. Reguzzoni and M. C. Righi, *Size dependence of static friction between solid clusters and substrates*, *Phys. Rev. B* **85** (May, 2012) 201412.

- [24] J. Gao, W. D. Luedtke, D. Gourdon, M. Ruths, J. N. Israelachvili and U. Landman, *Frictional forces and amontons' law: From the molecular to the macroscopic scale*, .
- [25] U. D. Schwarz, O. Zwörner, P. Köster and R. Wiesendanger, *Quantitative analysis of the frictional properties of solid materials at low loads. i. carbon compounds*, *Phys. Rev. B* **56** (Sep, 1997) 6987–6996.
- [26] S. Li, Q. Li, R. W. Carpick, P. Gumbsch, X. Z. Liu, X. Ding et al., *The evolving quality of frictional contact with graphene*, .
- [27] J. Tersoff, *New empirical approach for the structure and energy of covalent systems*, *Phys. Rev. B* **37** (Apr, 1988) 6991–7000.
- [28] S. Corporation, “pair_style lj/cut command.”
- [29] X. Wang, S. Ramírez-Hinestrosa, J. Dobnikar and D. Frenkel, *The lennard-jones potential: when (not) to use it*, *Phys. Chem. Chem. Phys.* **22** (2020) 10624–10633.
- [30] R. Naeem, “Lennard-jones potential.”
- [31] Q. Zhang, D. Diao and M. Kubo, *Nanoscratching of multi-layer graphene by molecular dynamics simulations*, *Tribology International* **88** (2015) 85–88.
- [32] S. Corporation, “pair_style sw command.”
- [33] F. H. Stillinger and T. A. Weber, *Computer simulation of local order in condensed phases of silicon*, *Phys. Rev. B* **31** (Apr, 1985) 5262–5271.
- [34] S. Corporation, “pair_style tersoff command.”
- [35] T. Schneider and E. Stoll, *Molecular-dynamics study of a three-dimensional one-component model for distortive phase transitions*, *Phys. Rev. B* **17** (Feb, 1978) 1302–1322.